CrossMark

ORIGINAL PAPER

Quantification of fluid shear stress in bone tissue engineering scaffolds with spherical and cubical pore architectures

Feihu Zhao[1] · Ted J. Vaughan[1] · Laoise M. McNamara[1]

Abstract Recent studies have shown that mechanical stimulation, in the form of fluid perfusion and mechanical compression, can enhance osteogenic differentiation of mesenchymal stem cells and bone cells within tissue engineering scaffolds in vitro. The precise nature of mechanical stimulation within tissue engineering scaffolds is not only dictated by the exogenously applied loading regime, but also depends on the geometric features of the scaffold, in particular architecture, pore size and porosity. However, the precise contribution of each geometric feature towards the resulting mechanical stimulation within a scaffold is difficult to characterise due to the wide range of interacting parameters. In this study, we have applied a fluid–structure interaction model to investigate the role of scaffold geometry (architecture, pore size and porosity) on pore wall shear stress (WSS) under a range of different loading scenarios: fluid perfusion, mechanical compression and a combination of perfusion and compression. It is found that scaffold geometry (spherical and cubical pores), in particular the pore size, has a significant influence on the stimulation within scaffolds. Furthermore, we observed an amplified WSS within scaffolds under a combination of fluid perfusion and mechanical compression, which exceeded that caused by individual fluid perfusion or mechanical compression approximately threefold. By conducting this comprehensive parametric variation study, an expression was generated to allow the design and optimisation of 3D TE scaffolds and inform experimental loading regimes so that a desired level of mechanical stimulation, in terms of WSS is generated within the scaffold.

1 Introduction

The primary function of porous biomaterial scaffolds in tissue engineering (TE) applications is to enable cells to attach, migrate and proliferate, thereby providing a suitable environment to support tissue growth (Hutmacher 2000; Kim et al. 2010; Milan et al. 2010). This is facilitated through the use of highly porous scaffold architectures, which enable nutrient and metabolite diffusion throughout, while also contributing to the shape and mechanical integrity of the tissue defect. Mechanical stimulation, in the form of fluid perfusion and mechanical compression, has been shown to play an important role in enhancing tissue regeneration and also directing the cellular fate of mesenchymal stem cells (MSCs) (Angele 2004; Delaine-Smith and Reilly 2012; Jaasma and O'Brien 2008; Keogh et al. 2011; Liu 2012b; Miyashita 2014; Thompson et al. 2010). For example, osteogenic differentiation of MSCs is prompted under mechanical stimulation, as indicated by the increase in alkaline phosphatase (ALP), prostaglandin E_2 (PGE_2) expression and mineralisation (Bancroft et al. 2002; Grayson et al. 2008; Vance et al. 2005; Yu et al. 2004).

While the mechanical environment plays an important role in controlling the cellular fate of MSCs and enhancing tissue regeneration, the precise nature of mechanical stimulation (e.g. mechanical strain and fluid shear stress) within a scaffold is difficult to characterise. Nevertheless, recent studies have characterised the deformation of biomaterial scaffolds under compressive loading using experimental techniques (Bliss et al. 2007; Harley et al. 2007; Kerckhofs et al. 2010).

✉ Laoise M. McNamara
  laoise.mcnamara@nuigalway.ie

[1] Biomechanics Research Centre (BMEC), Biomedical Engineering, College of Engineering and Informatics, National University of Ireland, Galway, Ireland

However, direct measurement of fluid-induced shear stress within scaffolds is not feasible, which prevents researchers from correlating the levels of fluid shear stress to biochemical responses, see in particular (Gomes et al. 2003; Jagodzinski et al. 2008; Liu 2012a) and Table 1. Therefore, researchers are required to employ analytical predictions, based on idealised flow through a cylinder or two plates (Blecha et al. 2010; Goldstein et al. 2001), or estimate wall shear stress (WSS) magnitudes from existing computational models (Bancroft et al. 2002; Grayson et al. 2008; Vance et al. 2005; Yu et al. 2004), see Table 1. However, fluid shear stresses are not only dictated by the exogenously applied loading regime (Kim et al. 2010; Tai 2007; Widmer et al. 1998), but also depend on the geometric features of a particular scaffold (i.e. architecture, pore size and porosity), and the precise contribution of each towards the resulting mechanical stimulation within a scaffold is difficult to characterise due to the range of interacting parameters. While previous studies have characterised WSS as a function of architecture, pore size or porosity, the range of parameters considered in many of these studies is limited, with studies perhaps only considering a single pore size (McCoy et al. 2012) or porosity (Melchels et al. 2011), for example.

Several computational models have been developed that characterise mechanical stimulation within TE scaffolds under a range of experimental culture conditions (Hendrikson et al. 2014; Jungreuthmayer et al. 2009a, b; Marin and Lacroix 2015; McCoy et al. 2012; Porter et al. 2005; Tuan and Hutmacher 2005). For instance, a computational fluid dynamics (CFD) study showed that the wall shear stress (WSS) in collagen–glycosaminoglycan (GAG) scaffold (porosity = 99 %) was almost thirty-fold lower than that of a calcium phosphate (CP) scaffold (porosity = 60 %) and this could be explained by the difference in scaffold geometries (collagen–GAG pore size $d \approx 96\,\mu$m, CP pore size $d \approx 350\,\mu$m) (Jungreuthmayer et al. 2009a). To study the effect of scaffold pore size and applied loading on WSS at cellular level, McCoy et al. (2012) developed a fluid–structure interaction (FSI) model for collagen–GAG scaffolds with pore sizes of 85, 120 or 325 μm under applied fluid flow stimulation in the range of 0.05–5 mL/min. It was found that the applied flow rate dominated the mechanical stimulation when compared to the pore size. A computational study was carried out by Olivares et al. (Olivares et al. 2009), to investigate the influence of scaffold architecture (hexagon and gyroid), porosity (55 and 70 %) and applied loading (inlet fluid velocity: 100 and 1000 μm/s; compressive strain: 0.5 and 5 %) on the WSS and mechanical strain using CFD and finite element (FE) approaches. The results of this study predicted that the distribution of WSS induced by fluid perfusion was dependent on scaffold architecture. Furthermore, with the same porosity (55 %), the WSS in the gyroid architecture was twofold of that in the hexagonal architecture under a

constant fluid velocity (1 mm/s), and the WSS values were higher under fluid perfusion than mechanical compression. While these studies have provided an insight into the mechanical environment of TE scaffolds under external loading, the quantitative expressions of mechanical stimulation, in terms of WSS, with respect to scaffold geometry (i.e. architecture, pore size and porosity) are still unknown, which limits researchers to efficiently determine the resulting mechanical stimulation in their TE scaffolds.

A recent experimental study showed that a combination of applied fluid perfusion and mechanical compression resulted in increased cell proliferation and osteogenic activity (i.e. Runx2, ALP activity) when compared to applied fluid perfusion only (Jagodzinski et al. 2008; Liu 2012a; Stops et al. 2010). Interestingly, recent computational studies showed that a combination of fluid perfusion and mechanical compression led to more ubiquitous stimulation of bone cells within a TE scaffold (Hendrikson et al. 2014; Zhao et al. 2015), in particular to both cells that had an attached and bridged configuration. However, these studies only investigated a single loading regime and the nature of mechanical stimulation within scaffolds under different types of combined external loading (e.g. inlet fluid velocity and compressive strain) are still unknown.

Therefore, in this study, we aim to characterise the nature of WSS in a number of idealised scaffold architectures with spherical and cubical pores by developing an efficient computational method. These scaffolds are commonly used in tissue engineering studies, as the scaffolds with spherical and cubical pores are easily fabricated and controlled in pore size and porosity by particle leaching and fibre matrix techniques (Smith and Ma 2010; Tang et al. 2011). Furthermore, we carry out an extensive parameter variation study to characterise the combined effect of scaffold pore size, porosity and applied loading. This study strives to derive an analytical expression that can be applied to estimate magnitudes of WSS generated in bone TE scaffolds for a range of different scaffold geometries and experimental conditions.

2 Materials and methods

In this study, we develop computational fluid dynamics (CFD) and fluid–structure interaction (FSI) models to investigate the role of scaffold model geometry (i.e. architecture, pore size and porosity) on pore wall shear stress under a range of different loading scenarios.

2.1 Variation of scaffold geometries

This study investigated the influence of different scaffold architectures, pore sizes and porosities on predicted WSS within the scaffolds. The parameter variation study of pore

Table 1 Literature review of the mechanical stimulation in bone tissue engineering experiments

Scaffold				Cells	Loading		Results	Cell responses	References
Materials	Architecture	Pore size	Porosity (%)		Inlet fluid velocity (flow rate)	Compressive strain	Wall shear		
Native trabecular bovine bone	Irregular	600–1000 μm	70–80	Human mesenchymal stem cells (hMSCs)	100–400 μm/s	–	0.7–10 mPa	Higher DNA value of cells under higher flow rate; Improved mineralisation under higher flow rate after 5-week culture	1
Titanium fibre mesh	Irregular	250 μm	86	Marrow stromal osteoblast	0.3–3 mL/min	–	<100 mPa	Higher ALP activity under fluid perfusion than static culture; Highest mineralisation on 16-day culture under flow rate of 3mL/min	2
Calcium phosphate	Irregular	350 μm	67.5	MC3T3 osteoblastic cells	0.025 mL/min for 4h Oscillating flow: 40 mL/min 1 Hz for 30 min	–	0.7 mPa 1.2 Pa	Greater increase in PEG2 under constant flow than static culture; Greatest increase in PEG2 is under the oscillating flow after 24- and 48-h culture	3
Poly (lactide-co-glycolide) (PLGA)	Spherical	425–500 μm	–	Rat calvarial osteoblastic cells	48.9–103.1 mm/s	–	160–320 mPa	Increased ALP activity, osteocalcin expression and mineralisation after both 4-day and 7-day culture	4
SEVA-C-based polymer scaffolds SPCL fibre mesh scaffold	Irregular	181 μm	75 60	Rat bone marrow cells	0.3 mL/min	–	–	No significant difference of ALP activity between perfusion and static culture in SPCL fibre mesh after 15 days; Higher AP activity in SEVA-C scaffold under perfusion than static culture after 15 days; A dramatic increase in calcium deposition in both scaffolds under perfusion than static culture after 15 days	5
Polyurethane (PU)-based 1, 4-butanediisocyanate (BDI)	Spherical	80–400 μm (226 μm in average)	81	Human bone marrow stromal cells (hBMSC)	10 mL/min	10% 0.5-Hz stimulation 1 time/day, 8h/time	–	I: After 2-week culture by stimulation I: 1.85-fold increase in equilibrium modulus, 3.25-fold increase in procollagen produced by MSCs. After 2-week culture by stimulation II: 2.02-fold increase in tensile modulus, 2.24-fold increase in procollagen produced by MSCs	6

Table 1 continued

Scaffold				Cells	Loading		Results		References
Materials	Architecture	Pore size	Porosity (%)		Inlet fluid velocity (flow rate)	Compressive strain	Wall shear	Cell responses	
Bovine spongiosa disc	Irregular	–	–	hBMSC	Group A: 10 mL/min Group B: 10 mL/min	Stimulation II: 4 times/day, 2 h/time, 4-h rest Group A: Group B: 10%, 0.5 Hz	–	Upregulated Runx2 mRNA in both Groups A and B after 1, 2 and 3 weeks compared to static culture Higher amount of osteocalcin in Group B	7

1 Grayson et al. (2008), *2* Bancroft et al. (2002), *3* Vance et al. (2005), *4* Yu et al. (2004), *5* Gomes et al. (2003), *6* Liu (2012a), *7* Jagodzinski et al. (2008)

size and porosity was carried out on scaffolds with two regular architectures (spherical and cubical) based on those commonly used are TE studies (see Fig. 1) (Bose et al. 2013; Gross and Rodriguez-Lorenzo 2004; Hollister 2005; Shin et al. 2012; Tai 2007; Widmer et al. 1998). The scaffolds had a uniform length and thickness of 8 and 4 mm, respectively, and were built from repeating units with spherical and cubical pores as shown in Fig. 1. By geometric analysis, we obtained the following formulas showing the relationship between the porosity, pore size and the length of repeating unit, based on which the model geometries could be determined.

For a spherical architecture:

$$p = -\frac{\pi}{3} \cdot \left(\frac{d}{L}\right)^3 + \frac{3\pi}{4} \cdot \left(\frac{d}{L}\right)^2 - \frac{\pi}{4}; \tag{1}$$

For a cubical architecture:

$$p = -2\left(\frac{d}{L}\right)^3 + 3\left(\frac{d}{L}\right)^2, \tag{2}$$

where p was porosity, d was pore size (i.e. diameter of the spherical pore and the length of the cubical pore), and L was the length of repeating unit as shown in Fig. 1.

Due to the repeating nature of the scaffold architecture, central regions of 0.5–1.905 and 0.5–2.116 mm were modelled for spherical-architecture and cubical-architecture scaffolds, respectively (see Fig. 1), to ensure that every model had more than 3×3 repeating units in one cross section. It is important to note the pore size (d) and porosity (p) parameters were varied independently of one another, whereby these variables were defined as $d = 100$–$400\,\mu$m and $p = 60$–$90\,\%$ in increments $50\,\mu$m and $5\,\%$, respectively. According to Eqs. 1 and 2, the values of scaffold geometric parameters were obtained and formulated into ANSYS parametric design. For the porosity (p) variation, the pore size (d) was assumed as constant, and the length of repeating unit (L) was varied, as described in Eqs. 1 and 2. Similarly, for the pore size variation, the porosity was held constant, and the length of repeating unit was varied.

2.2 Material and fluid properties

The geometric variation study was based on scaffolds fabricated from poly(D,L-lactide) (PDLLA) material, which had a Young's modulus and Poisson's ratio of 3.3 GPa and 0.3, respectively (Olivares et al. 2009). Due to the high Young's modulus, the influence of fluid on the scaffold deformation was neglected for perfusion flow, meaning the effect of geometric parameters could be characterised using a CFD model. Therefore, the scaffold geometric variation under the fluid perfusion loading was conducted using a CFD model. The perfusion medium (Dulbecco's modified Eagle medium:
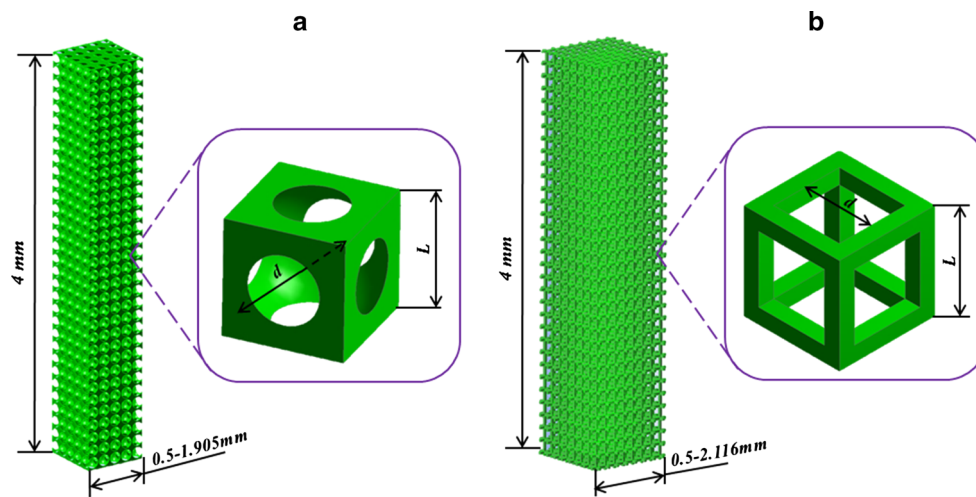
Fig. 1 Geometries of the scaffolds with **a** spherical architecture and **b** cubical architecture

DMEM) was modelled as Newtonian fluid with dynamic viscosity of $\mu = 1.45$ mPa s and a density of $\rho = 1000$ kg/m^3 (Olivares et al. 2009).

2.3 Boundary and loading conditions of computational fluid dynamics model

A constant uniform inlet fluid velocity profile was applied (v $= 100\,\mu$m/s), and a zero pressure boundary condition was assumed at the outlet (Gomes et al. 2003; Zhao et al. 2015). A non-slip wall boundary condition was applied to the scaffold surfaces as shown in Fig. 2a, and four side faces were defined as symmetric boundaries, specifically:

$$v_j \frac{\partial v_i}{\partial x_j} = 0 \quad (j = 1, 2) \tag{3}$$

where v_i was the fluid velocity, v_j the velocity components in Cartesian co-ordinates, and x_j were on the symmetric boundaries $\Gamma_s : x_j \in \Gamma_s$.

The flow regime was determined based on Reynolds number (Re), which was estimated by Eq. (4):

$$\text{Re} = \frac{\rho v d}{\mu} \tag{4}$$

The Reynolds numbers were obtained in the range of 0.0067–0.027, which was much smaller than the critical value of 2000, indicating that the flow regime could be assumed to be laminar. Furthermore, a mesh refinement study was carried out for two cases of scaffold porosity ($d = 100\,\mu$m, $p = 60\%$ and $d = 400\,\mu$m, $p = 90\%$), and it was determined that a global quadratic tetrahedral element size of $50\,\mu$m was suitable in the main volume regions, while the mesh size on scaffold surfaces was refined to an approximate element size of $10\,\mu$m. Finally, the ANSYS CFX solver resolved the models using a finite volume method under the root-mean-square (RMS) residual convergence criteria of 1×10^{-4}.

2.4 Boundary and loading conditions of fluid–structure interaction model

In the mechanical compression system, an FSI model was used to investigate the influence of scaffold geometry on resulting WSS imparted of scaffold surfaces. A compressive strain of 5% was applied on the top surface of the scaffold at a frequency of 1 Hz, as shown in Fig. 2b. The side and bottom faces of the scaffolds were as assigned a frictionless support, and specifically, the displacements in Cartesian co-ordinate were $z = 0$ for the bottom face and $x = y = 0$ for the side surfaces in Fig. 2b. The scaffold inner surfaces formed the fluid–structure interface. The deformation of scaffolds was computed by the ANSYS structural solver under transient state.

The model was based on a specific bioreactor design, in which the fluid could freely transport through the scaffold ends under mechanical loading, and the scaffold was laterally confined (Chowdhury et al. 2010; Schulz et al. 2008). Therefore, the inlet and outlet of the scaffold were assumed as opening boundaries with a pressure of 0 Pa, facilitating inward and outward flow. Furthermore, four side faces were set as symmetric boundaries. The inner surfaces of the fluid domain, which interacted with the scaffold, were defined as non-slip fluid–structure interface as expressed in Eqs. 5 and 6 (Hou et al. 2012). A two-way FSI analysis was carried out, which used a staggered iteration approach, whereby the pressure and velocity fields were resolved in the fluid domain. The fluid stress tensor was applied to the fluid–solid interface, and the deformation of scaffold was relayed back to the fluid domain (Hou et al. 2012). Therefore, at the fluid–solid interface, the following conditions apply,
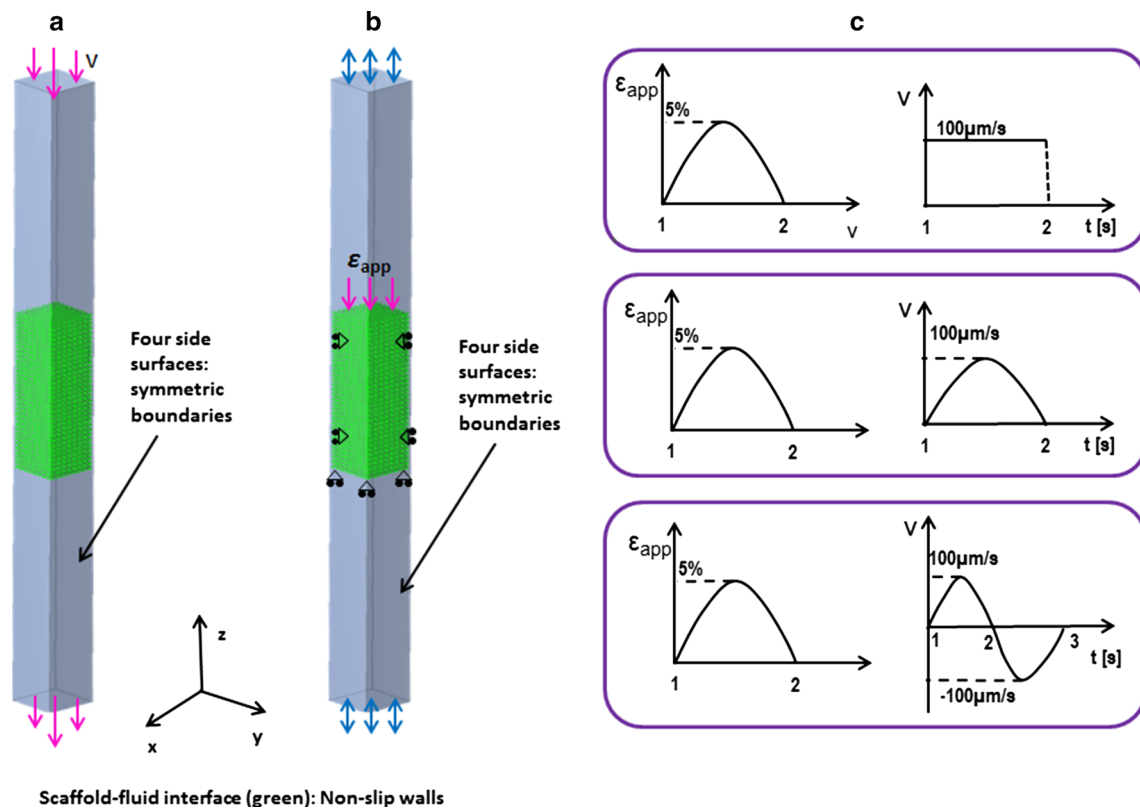
Fig. 2 Boundary and loading conditions of **a** computational fluid dynamics model for fluid perfusion system; **b** fluid–structure interaction model for mechanical compression system; **c** combined applied loading profiles: a pulsatile compression with the strain (ε_{app}) magnitude of 5 %

(1 Hz) is combined with a constant inlet fluid velocity (v) of $100\,\mu\text{m/s}$, a pulsatile fluid velocity with the magnitude of $100\,\mu\text{m/s}$ (1 Hz) and a cyclic fluid velocity with the magnitude of $100\,\mu\text{m/s}$ (0.5 Hz)

$$v_i^s = v_i^f \tag{5}$$

$$\sigma_{ij}^s \cdot n_i = \sigma_{ij}^f \cdot n_i \tag{6}$$

$$u_i^s = u_i^f \tag{7}$$

where the superscripts s and f represented the solid (scaffold) and fluid domains; v_i and u_i were velocity components, respectively; $\sigma_{ij} \cdot n_i$ was the normal stress tensor.

The mesh was generated on the solid domain with a minimum length size of $9.5\,\mu\text{m}$ by a quadratic tetrahedron method with a patch conforming algorithm. The CFD domain was meshed to the same resolution as those described above for the fluid perfusion CFD model. The model was resolved in transient state by the ANSYS CFX solver under the RMS residual convergence criteria of 1.0×10^{-4}.

2.5 Combined loading

Finally, the applied loading conditions (i.e. inlet fluid velocity and compressive strain) were varied to determine their effect of WSS. This was carried out for a PDLLA scaffold

that had a spherical architecture, with a pore size of $300\,\mu\text{m}$ and porosity of 90 % (Blecha et al. 2010; Bose et al. 2013; Georgiou et al. 2007; Karande et al. 2004; Silva 2006; Tan et al. 2011). Firstly, we investigated the influence of inlet fluid velocity on the WSS using the similar FSI model to that described in Sect. 2.4. The variation of inlet fluid velocity was achieved by applying three different fluid patterns (i.e. constant, pulsatile and cyclic) as shown in Fig. 2c. This was a transient analysis that used a coupling time step of 0.05 s, and pressure and velocity fields were solved using the ANSYS CFX solver under the RMS residual convergence criteria of 1.0×10^{-4}.

With a similar FSI model, a study of the combined loading (perfusion and compression) was carried out. As shown in Fig. 2c, three types of loading were applied to the scaffold, which were combinations of the pulsatile compression of magnitude 5 % (1 Hz) with: (i) the constant inlet fluid velocity of $100\,\mu\text{m/s}$, (ii) the pulsatile inlet fluid velocity with a magnitude of $100\,\mu\text{m/s}$ (1 Hz) and (iii) the cyclic inlet fluid velocity with a magnitude of $100\,\mu\text{m/s}$ (0.5 Hz).
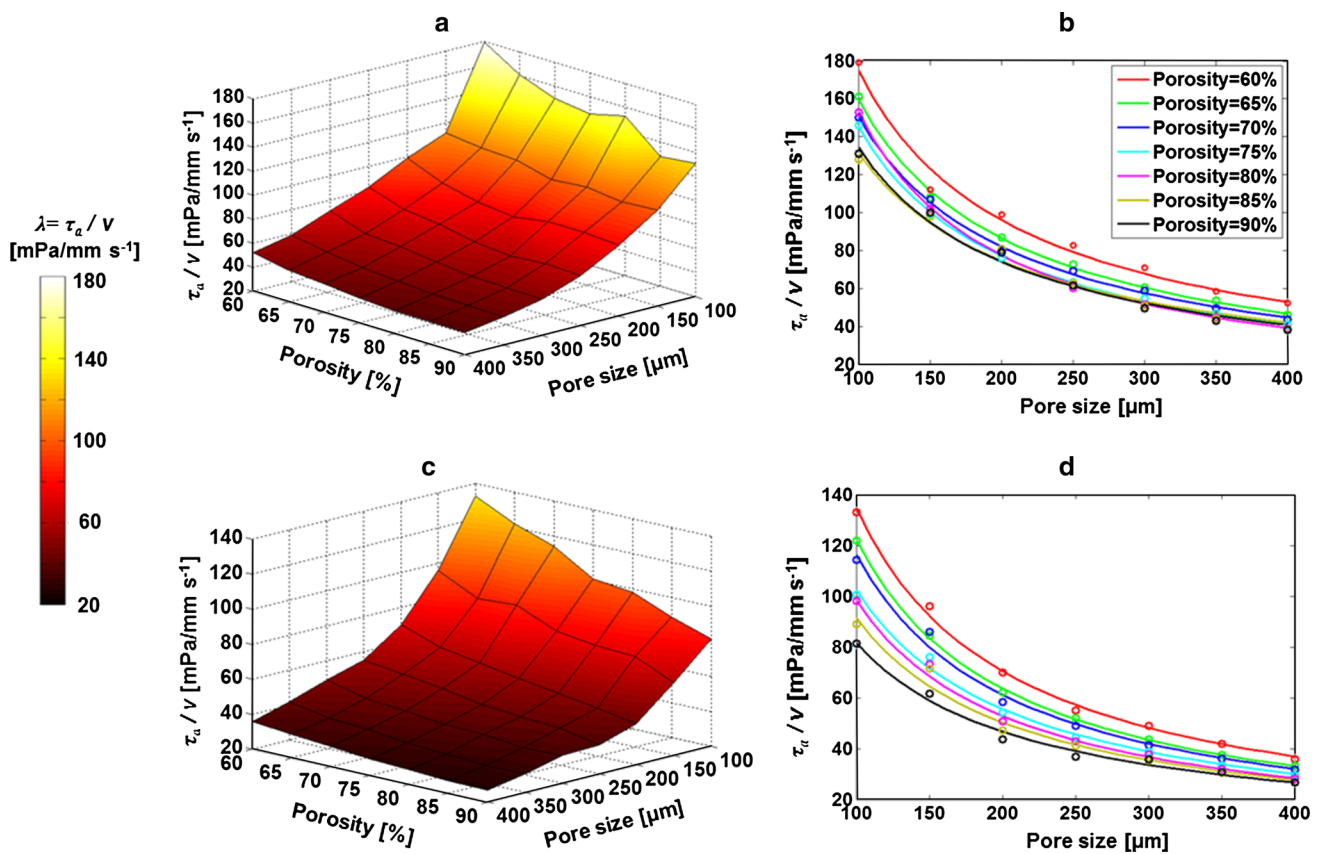
Fig. 3 **a** Ratio (λ) between average wall shear stress and inlet fluid velocity (τ_a/v) with respect to pore size (d) and porosity (p) of spherical-architecture scaffold under fluid perfusion; **b** computational results of λ that is fitted by power functions; **c** ratio (τ_a/v) with respect to pore size (d) and porosity (p) of cubical-architecture scaffold under fluid perfusion; **d** computational results of $\lambda = \tau_a$/v that is fitted by power functions

3 Results

3.1 Fluid perfusion

The geometric variation study characterised the effect of pore size, porosity and scaffold architecture on WSS under both fluid perfusion and load-induced fluid flow due to mechanical compression. The resulting average WSS imparted on scaffold surfaces in the case of fluid perfusion was shown in Fig. 3. The average WSS was found to be proportional to the inlet fluid velocity, and the results shown in Fig. 3 were presented as a variable (λ), which defined the ratio between average WSS (τ_a) and inlet fluid velocity (v). It was found that all the investigated parameters, i.e. scaffold architecture, pore size and porosity, had an effect on the average WSS imparted on scaffold surfaces. The most influential parameter governing mechanical stimulation within a scaffold was its pore size (d), whereby the average WSS in smaller-pore scaffolds (i.e. $d = 100\,\mu$m) was approximately 3.3-fold higher than that of the larger ones (i.e. $d = 400\,\mu$m). For both spherical and cubical architectures, the average WSS decreased

with increasing pore size. In Fig. 3b, d, the results of the variable $\lambda(\tau_a$/v) with respect to pore size (d) were fitted by the following power function as shown in Fig. 3:

$$\lambda (d) = a \cdot d^b \tag{8}$$

wherein the detailed mathematical expressions and values of coefficients a_i, b_i and c_i are listed in Table 2.

Shown in Fig. 4 are the WSS and fluid velocity distributions within the unit scaffolds for pore sizes 250–350 μm (each has a porosity of 90 %), which are from the centre of the global scaffolds. The scaffold with a pore size of 250 μm experienced greater WSS magnitudes compared to either the 300- or 350-μm pore-sized scaffold, and this high WSS was concentrated in the intermediate region between two adjacent pores. Furthermore, as shown in Fig. 4d–f, the fluid velocity was higher in the scaffold with a pore size $d = 250\,\mu$m (v = 266 μm/s) than the scaffolds with pore sizes of $d = 300\,\mu$m and 350 μm (v $\approx$ 258 μm/s). Within these three scaffolds, high fluid velocity was concentrated at the pore connections along the longitudinal direction,

Table 2 Coefficients of power functions of λ (ratio between average wall shear and inlet fluid velocity) with respect to pore size (*d*) under fluid perfusion

$\lambda(d) = a \cdot d^b$

Architecture	Coefficient	Porosity						
		60 %	65 %	70 %	75 %	80 %	85 %	90 %
Spherical pore	a	9302	9335	8437	9669	14,160	5754	7086
	b	−0.8629	−0.8835	−0.8744	−0.9117	−0.9829	−0.8204	−0.8607
Cubical pore	a	9857	9308	8397	5963	6177	4839	3372
	b	−0.9325	−0.9409	−0.9291	−0.8826	−0.8969	−0.8617	−0.8077
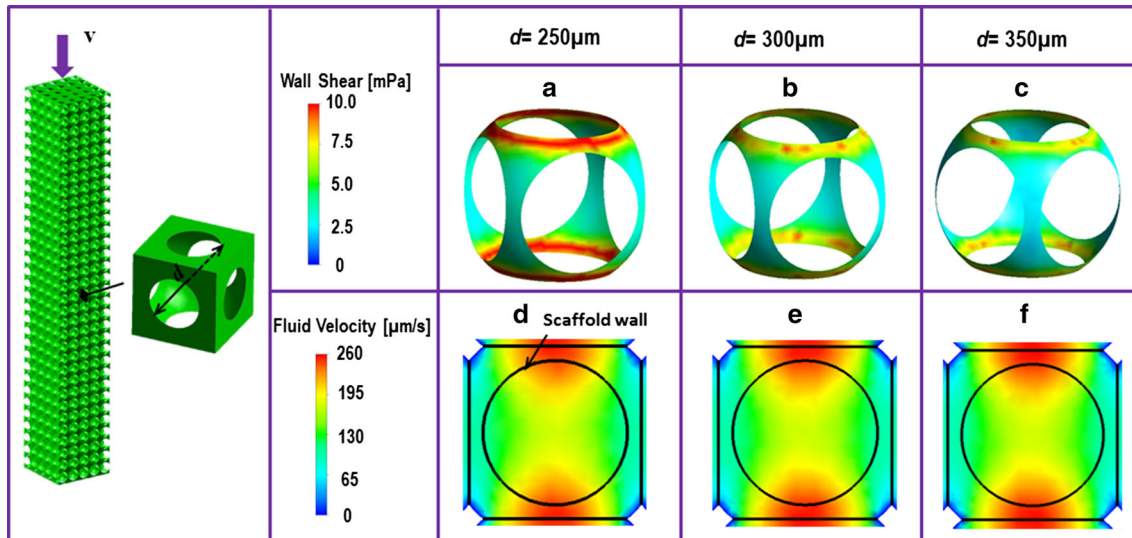
Fig. 4 In fluid perfusion system (inlet fluid velocity = 0.1 mm/s), wall shear stress (WSS) distribution within the scaffold units with spherical architecture, porosity of 90 % and pore size of **a** 250 µm, **b** 300 µm and **c** 350 µm; **d**–**f** fluid velocity distribution within the respective unit scaffolds

whereas in the transverse direction, the rate of fluid perfusion was not substantial.

For the cubical-architecture scaffold, the threshold pore size occurred at around 250 µm as shown in Fig. 3c, d. It was observed that the WSS also concentrated at the connections between each two pores; however, the magnitude was higher in the scaffold with pore size of 200 µm than that in the 250 µm and 300 µm ones (see Fig. 5a–c). Similar to the spherical architecture, the fluid velocity in cubical-architecture scaffolds also concentrated at the pore connections in the longitudinal direction and was of a similar magnitude (i.e. about 260 µm/s), whereas lower perfusion was observed in the transverse direction (Fig. 5d–f). The magnitude of WSS was not different between cubical- and spherical-architecture scaffolds.

The WSS distribution within cubical and spherical scaffolds of pore sizes 200–350 µm (each has a porosity of 90 %) is shown in Fig. 6. The WSS was more equally distributed within spherical-architecture scaffolds than within cubical architectures. For example, for a scaffold with a pore size $d = 300$ µm, approximately 84.7 % of the cubical surface area was exposed to a WSS range of 0–8 mPa, whereas 94.5 % of the spherical scaffold surface area was within a narrower range of WSS (i.e. 2–8 mPa). More interestingly, it was found that a larger pore size could lead to a more equally distributed WSS for both spherical and cubical architectures. For instance, for scaffolds with a pore size of 300 µm, 99.3 % (spherical architecture) and 99.1 % (cubical architecture) of the surface area had WSS in the ranges of 2–10 and 0–10 mPa, respectively. For the scaffolds with a pore size of 250 µm, a smaller surface area (i.e. 88.4 % of spherical architecture and 92.2 % of cubical architecture) was exposed to similar WSS ranges.

3.2 Load-induced fluid flow under mechanical compression

In this parameter variation study, the influence of load-induced fluid flow, which resulted from externally applied mechanical compression, on WSS imparted on scaffold surfaces was investigated using a two-way FSI model. Here, the resulting average WSS was found to be proportional
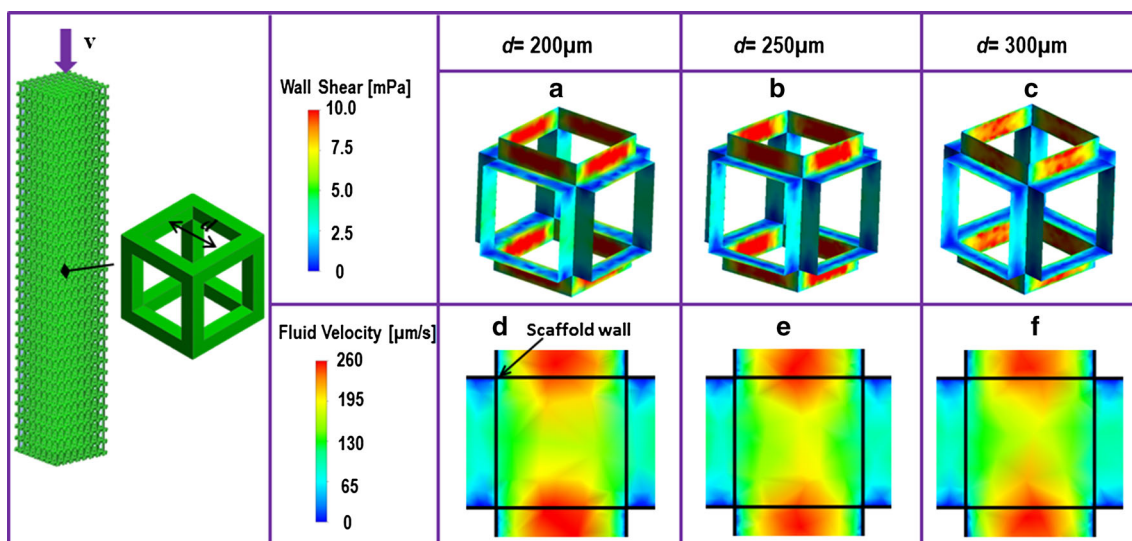
Fig. 5 In fluid perfusion system (inlet fluid velocity = 0.1 mm/s), wall shear stress (WSS) distribution within the scaffold units with cubical architecture, porosity of 90% and pore size of **a** 200 μm, **b** 250 μm and **c** 300 μm; **d–f** fluid velocity distribution within the respective unit scaffolds
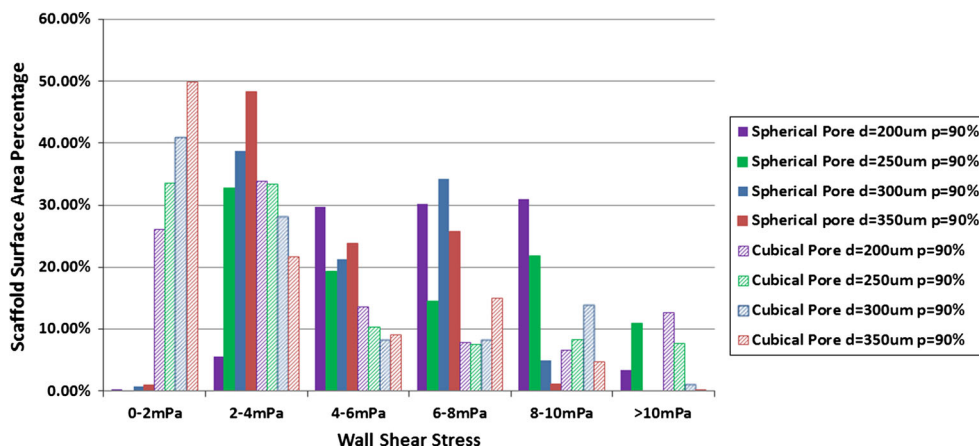

Fig. 6 Wall shear stress distribution in spherical- and cubical-architecture scaffolds with the porosity of 90% and pore sizes of 200–350 μm

to the magnitude of compressive strain under the loading frequency of 1 Hz. We therefore implemented another variable (β) to represent the ratio between average scaffold WSS (τ_a) and applied compressive strain (ε_{app}). Under mechanical compression, the average WSS in the spherical scaffold was approximately 1.5-fold higher than the cubical scaffold (Fig. 7a, c). A variable $\beta(\tau_a/\varepsilon_{app})$ with respect to pore size (d) was derived for each porosity, as described by mathematical expressions in Table 3. In this case, it was found that the pore size was the most critical parameter for determining the average WSS imparted on the scaffold surfaces, with smaller pore sizes leading to higher average WSS values, as shown in Fig. 7. The effect of porosity on resulting WSS in both scaffold architectures was found to be relatively small, as shown in Fig. 7.

Shown in Fig. 8 are the WSS and fluid velocity distributions (at time = 1.25s) within the spherical-architecture

scaffolds that had pore sizes of 200–300 μm, each having a porosity of 90%. The scaffold with a pore size (d) of 200 μm showed higher WSS magnitude than those with $d = 250$ and 300 μm. Moreover, it was observed that the WSS in the centre of the scaffold reduced to zero and increased to a maximum level towards the opening boundaries at each end of each scaffold. Similar to the fluid perfusion case, the local WSS elevations were concentrated in the intermediate regions between two adjacent pores, as shown in Fig. 8a–c. Furthermore, at the time of 1.25s, when the WSS researched its maximum level, the fluid velocity concentrated in the area close to the scaffold end, which had a frictionless support boundary (see Fig. 8d–f). Moreover, the magnitude of fluid velocity was higher in the scaffold with a pore size of 200 μm compared to those with larger pore sizes (i.e. $d = 250$ and 300 μm).
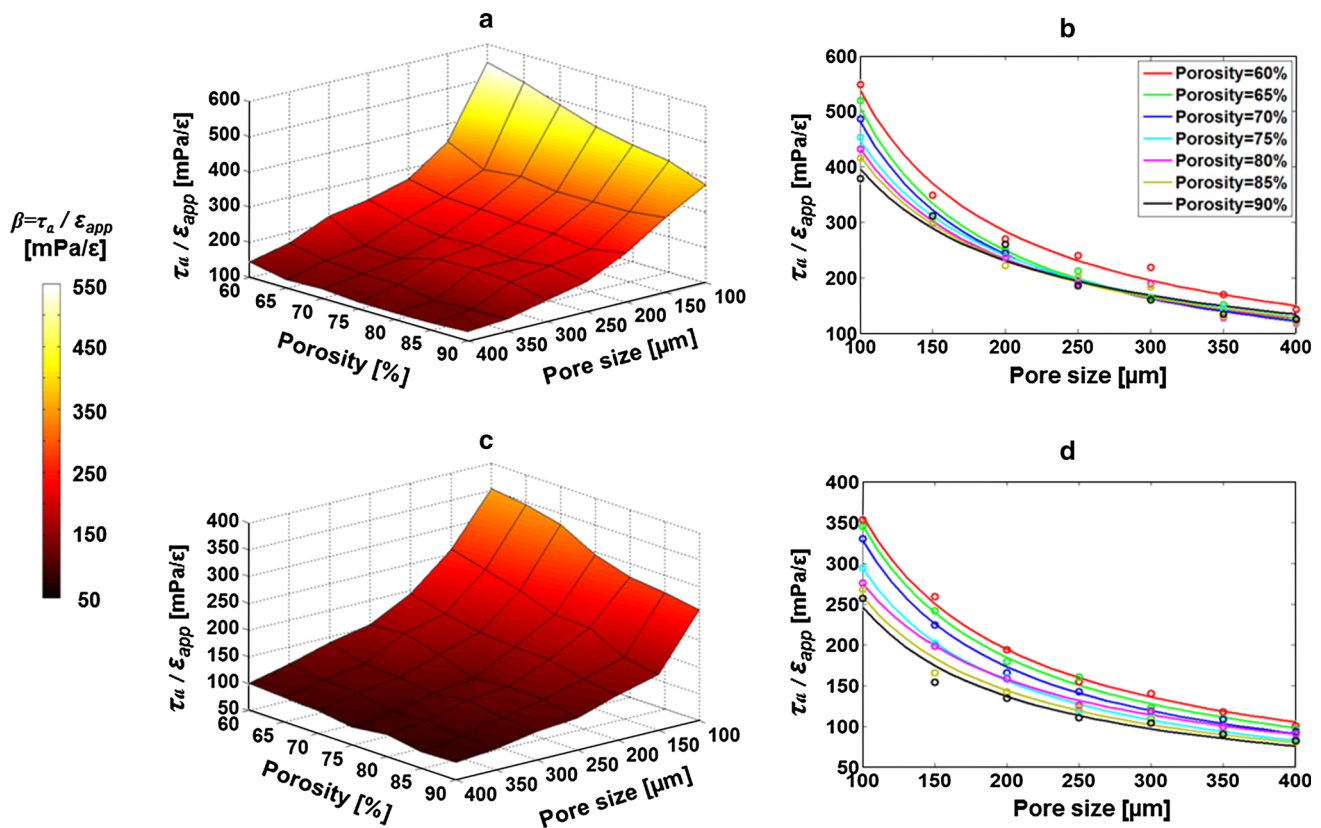
Fig. 7 **a** Ratio (β) between average wall shear stress and compressive strain (τ_a/ε_{app}) (frequency = 1 Hz) with respect to pore size (d) and porosity (p) of spherical-architecture scaffold under mechanical compression; **b** computational results of $\beta = \tau_a/\varepsilon_{app}$ that is fitted by power functions; **c** ratio (β) between average wall shear stress and compressive strain (τ_a/ε_{app}) (frequency = 1 Hz) with respect to pore size (d) and porosity (p) of cubical-architecture scaffold under mechanical compression; **d** computational results of $\beta = \tau_a/\varepsilon_{app}$ that is fitted by power functions

Table 3 Coefficients of power functions of β (ratio between average wall shear and compressive strain) with respect to pore size (d) under mechanical compression

$\beta(d) = a \cdot d^b$								
Architecture	Coefficient	Porosity						
		60 %	65 %	70 %	75 %	80 %	85 %	90 %
Spherical pore	a	37,370	55,430	45,610	27,630	25,200	20,820	14,370
	b	−0.9211	−1.020	−0.9884	−0.8953	−0.8831	−0.8488	−0.7797
Cubical pore	a	20,700	22,550	22,920	19,800	11,060	12,980	12,340
	b	−0.8812	−0.9080	−0.9233	−0.9142	−0.8023	−0.8498	−0.8499

Shown in Fig. 9a–c are the WSS distributions within the cubical-architecture scaffolds that had pore sizes of 200–300 μm, each having a porosity of 90 %. Similar to the spherical architecture, the WSS also concentrated in the intermediate regions between two adjacent pores (see Fig. 9a–c); moreover, the higher WSS magnitude was also observed in the scaffold with a pore size of 200 μm. In addition, similar fluid velocity distributions, as those in the spherical architecture, were found in the cubical-architecture scaffolds (Fig. 9d–f), wherein the fluid velocity concentrated in the area close to the end (frictionless support boundary), and it was minimised within the scaffold with a large pore size (i.e. $d = 300$ μm). However, the magnitude of fluid velocity in cubical-architecture scaffold was lower than that in the spherical architecture.

3.3 External loading variation

For the fluid perfusion system, the average WSS within the spherical-architecture scaffold (pore size: $d = 300$ μm,
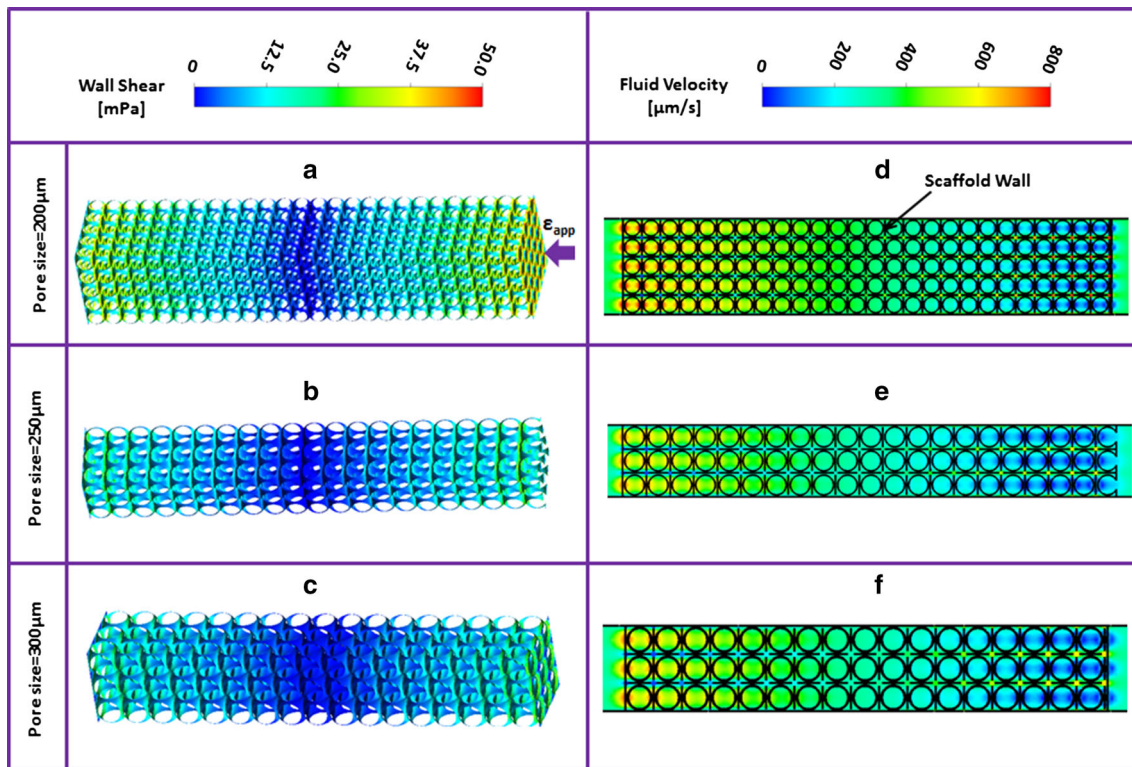
Fig. 8 At the time point ($t = 1.25$ s) with peaked wall shear stress (WSS) in mechanical compression system (compressive strain $= 5\%$, frequency $= 1$ Hz), WSS distribution within the spherical-architecture scaffolds with porosity of 90 % and pore size of **a** 200 μm, **b** 250 μm and **c** 300 μm; **d**–**f** fluid velocity distribution within the respective scaffolds

porosity: $p = 90\%$) was 4.96 mPa under a constant inlet fluid velocity of 100 μm/s. When pulsatile fluid velocity profiles were considered, the resulting average WSS showed the same patterns with the inlet flow and had a magnitude of 4.96 mPa (at peak flow). The magnitude of average WSS within the scaffolds was found to be proportional to the applied inlet fluid velocity ($\lambda = 49.6$ mPa/mm s^{-1}). Under mechanical compression, the resulting average WSS (τ_a) as shown in Fig. 10a had two peaks within one period (1–2 s), which could be described by a Fourier series as shown in Eq. 9. Furthermore, the average WSS (τ_a) is proportional to the loading rate of compressive strain (ε_{app}).

$$\tau_a = \sum_{i=0}^{N} a_i \cdot \cos(i \cdot \omega \cdot t) + b_i \cdot \sin(i \cdot \omega \cdot t) \qquad (9)$$

where the value of N and coefficients ω, a_i and b_i are listed in Table 4.

In addition, a combined loading of fluid perfusion and mechanical compression was applied to the scaffold as shown in Fig. 10b–d. The resulting average WSS also could be fitted by a Fourier series described by Eq. 9 with the coefficient a_i, b_i and ω listed in Table 4. When the resulting average WSS in combined loading system was compared to the average

WSS for either fluid perfusion or compression, it was found that the applied fluid flow played a more significant role in dictating the magnitude of resulting WSS, while compression determined the patterns of resulted WSS in a combined loading system. More interestingly, the WSS was amplified under the combined loading, instead of a simple superposition of the WSS results from the isolated fluid perfusion and mechanical compression systems.

4 Discussion

In this study, the influence of scaffold geometry and the applied loading regime on mechanical stimulation within two distinct TE scaffold architectures was investigated using CFD and two-way coupled FSI approaches. Our results showed that (i) the geometry of scaffold dominated the levels of mechanical stimulation within the scaffold and (ii) a combined loading regime (fluid perfusion and mechanical compression) would cause an amplified WSS, rather than a simple superposition from the isolated fluid perfusion and mechanical compression systems.

One limitation of this study was that due to computational limitations, the combined loading variation was based on
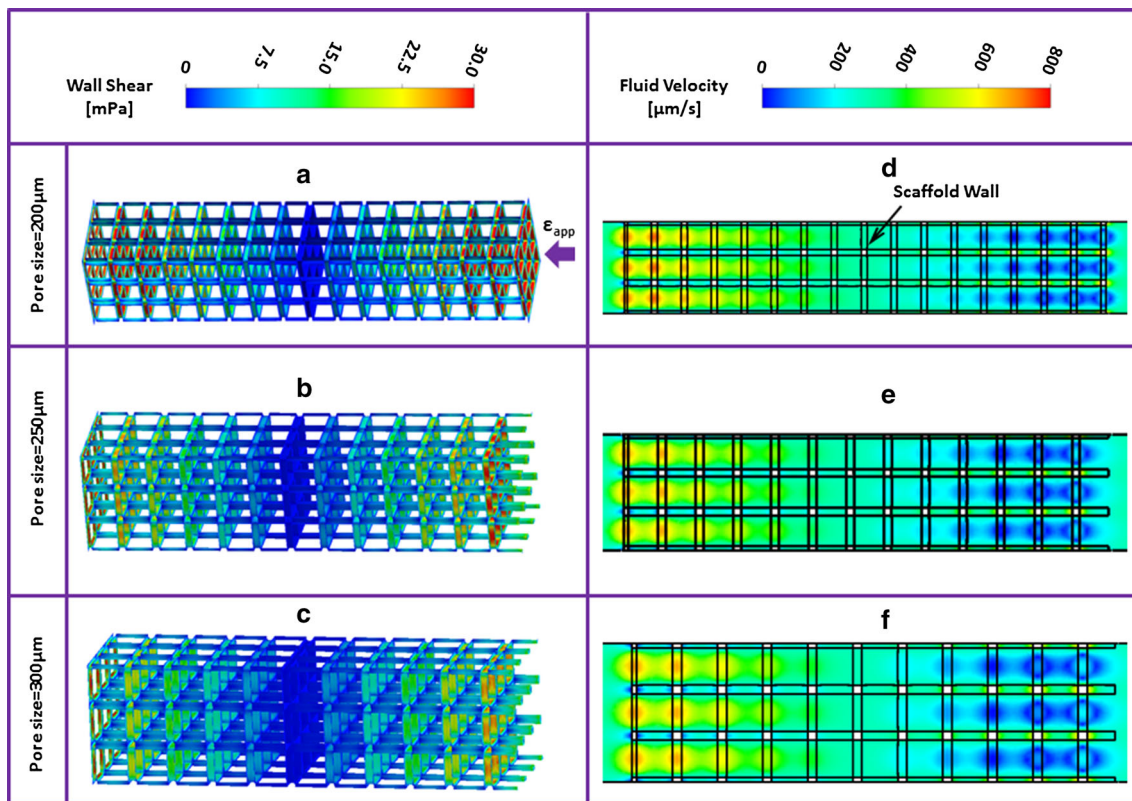
Fig. 9 At the time point ($t = 1.25$ s) with peaked wall shear stress (WSS) in mechanical compression system (compressive strain $= 5\%$, frequency $= 1$ Hz), WSS distribution within the cubical-architecture scaffold with porosity of 90 % and pore size of **a** 200 μm, **b** 250 μm and **c** 300 μm; **d–f** fluid velocity distribution within the respective scaffolds

one scaffold geometry for each of the spherical and cubical architectures, rather than a global parametric variation study including all of the geometries. However, the information predicted through these studies enables an enhanced understanding of the change of WSS under different types of combined loadings. Secondly, as the measurement of fluid-induced shear stress within scaffolds was still impossible using experiment techniques, this study focused on predicting the change in WSS as a function of scaffold geometry and the applied loading regime, to allow researchers to easily estimate the WSS generated within scaffolds. Therefore, the strain imparting a direct stimulus to cells adhered on the scaffold surface from the mechanical loading was not considered in this study. And thirdly, the parametric variation was implemented with cell-free scaffolds, so the WSS presented in this study was at the scaffold level. However, our previous study found that the WSS was amplified on cell surfaces, compared to the scaffold surfaces (i.e. the maximum: fivefold) (Zhao et al. 2015). Moreover, cells with different attachment types (attached on the struts and bridged across the pores) were found to receive different levels of strain under mechanical compression (Zhao et al. 2015). Furthermore, the modelling approach did not incorporate the effect of cell con-

traction, which was dictated by the mechanical properties of the biomaterial scaffold and influenced osteogenic differentiation (Harley et al. 2008; Keogh et al. 2010; Murphy et al. 2012, 2013). Cell contraction of biomaterial substrates has been modelled using computational approaches for individual cells (Dowling and McGarry 2014; Mullen et al. 2015, 2014), but it has not yet been achieved at the level of a three-dimensional scaffold due to the computational complexity of this problem. Finally, although this study considers regular architectures, Marin and Lacroix (2015) have recently shown that when these regular scaffolds are fabricated using rapid prototyping techniques, small variations in geometry post-fabrication can have a significant effect on generated mechanical stimulation due to flow perfusion. Based on the findings in (Marin and Lacroix 2015), it may be the case that local variations in WSS may actually be much higher due to manufacturing inconsistencies. Therefore, in future work, an investigation of the cellular-level mechanical stimulation within a realistic scaffold with attached cells could be carried out using an FSI approach to compare to the stimulation predicted here.

The key contribution of this study is the provision of a convenient mathematical expression that can be applied
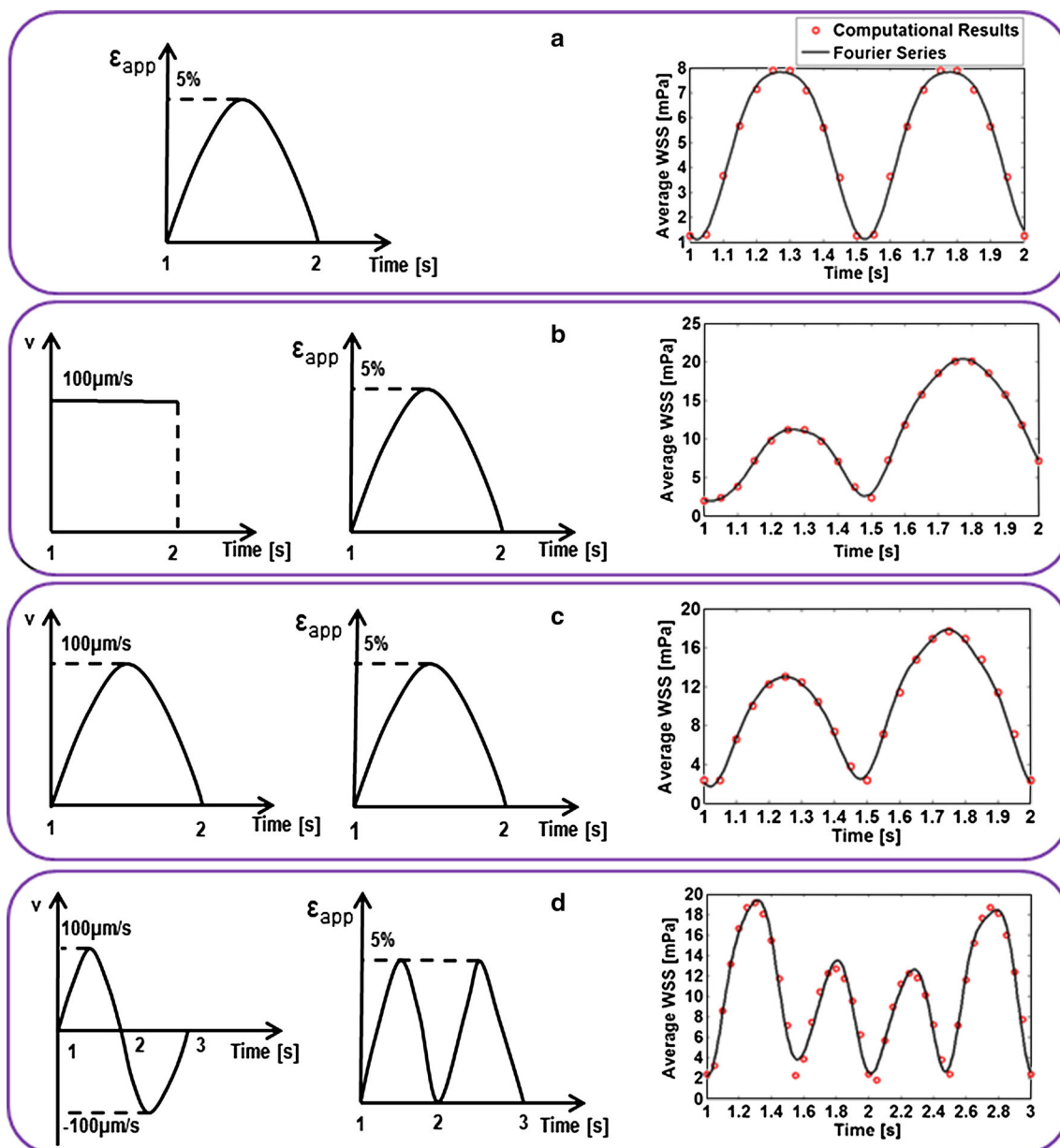
Fig. 10 Average wall shear stress within the spherical-architecture scaffold with the pore size of $300\,\mu m$ and porosity of $90\,\%$ under **a** pulsatile compression only, **b** constant flow and pulsatile compression, **c** pulsatile flow and pulsatile compression, **d** cyclic flow and pulsatile compression

by experimental researchers to estimate shear stress generated within their own scaffolds, based on experimental variables such as porosity, pore size and architecture, and thereby allow them to tailor their mechanical stimulation approach to optimise the likelihood of achieving the desired tissue differentiation. While other studies have characterised WSS as a function of architecture, pore size or porosity, the range of parameters considered in many of these studies is limited, with studies only considering a single pore size (McCoy et al. 2012) or porosity (Melchels et al. 2011), for example. Our study is the first to consider the combined effects of each of these parameters by independently vary-

ing each one over quite a wide range (similar to what has been used experimentally). This has important implications as there is an ever-increasing focus within the tissue engineering community to understand the role of mechanical loading for directing differentiation of mesenchymal stem cells and promoting cellular activity, in the form of proliferation, migration and ECM deposition (Altman 2002; Karamichos et al. 2008; Subramony et al. 2013; Wang and Chen 2013). For example, mechanical stimulation in the form of WSS that was in the range of 0.1–10 mPa was suggested for promoting osteogenic differentiation of mesenchymal stem cells, while WSS between 10 and 30 mPa

Table 4 Coefficients of Fourier series expressions of average wall shear stress (τ_a) under four types of loads

Coefficients	$\tau_a = \sum_{i=0}^{N} a_i \cdot cos\,(i \cdot \omega \cdot t) + b_i \cdot sin\,(i \cdot \omega \cdot t)$			
	Pulsatile compression only	Pulsatile compression and constant fluid flow	Pulsatile compression and pulsatile fluid flow	Pulsatile compression and cyclic fluid flow
N	2	6	6	8
ω	12.5	5.733	6.286	3.129
a_0	5.089	10.07	10.04	10.290
a_1	−3.268	−4.589	−0.3393	−2.712
a_2	−0.5637	−0.868	−6.101	−0.771
a_3	0	−1.134	−0.0494	2.814
a_4	0	0.6294	−1.028	−5.920
a_5	0	−0.1197	0.02893	−0.712
a_6	0	−0.2175	−0.3458	−0.3515
a_7	0	0	0	0.6797
a_8	0	0	0	−0.8477
b_1	−0.7018	−3.027	−2.823	−0.3428
b_2	−0.250	5.971	0.06703	−0.0446
b_3	0	0.0176	−0.7583	0.1997
b_4	0	−0.1871	−0.04379	−1.228
b_5	0	0.3102	−0.3647	−0.2638
b_6	0	−0.2625	−0.04111	−0.09039
b_7	0	0	0	0.1661
b_8	0	0	0	−0.3657

enhanced chondrogenesis (Olivares et al. 2009). Considering these stimulation thresholds and our model predictions, we propose that the inlet fluid velocity applied to spherical- and cubical-architecture scaffolds ($d = 300\,\mu$m, $p = 90\,\%$) should not exceed 0.20 and 0.28 mm/s, respectively, in order to achieve a WSS that would give rise to osteogenic differentiation (0.1–10 mPa). Similarly, an inlet fluid velocity within the range of 0.20–0.60 mm/s (spherical architecture) and 0.28–0.84 mm/s (cubical architecture) might be preferable for cartilage differentiation, and in excess of these, would likely lead to fibrous-tissue differentiation within either scaffold. This would have important practical implications for design of bioreactor experiments as such high velocities could result in the detachment of the cells (McCoy et al. 2012). For instance, it was observed that approximately 11.26 and 29.19 % of cells in a collagen–GAG scaffold (pore size $d = 120\,\mu$m) would be detached under the flow rate of 0.05 and 1 mL/min, respectively (McCoy et al. 2012). To achieve an average WSS of 5 mPa in scaffolds ($d = 120\,\mu$m), the applied inlet fluid velocity should be higher than 0.033 mm/s (flow rate = 0.127 mL/min) and 0.05 mm/s (flow rate = 0.192 mL/min) for spherical and cubical architectures, respectively. However, approximately 11.26 % of cells would be detached under such fluid velocities.

In the case of load-induced fluid flow resulting from mechanical compression, it was found that the scaffold WSS above certain loading cases would be higher than the threshold for bone cell differentiation. Typically, WSS resulting from load-induced fluid flow is not considered to be the main driver of scaffold stimulation under compressive loading regimes (Sandino et al. 2008; Zhao et al. 2015). However, our model predicts that under a compressive strain of 5 % (1 Hz) in 400-μm pore-sized scaffolds, which has been experimentally shown to achieve enhanced osteogenic differentiation (i.e. higher ALP, osteopontin expression and calcium content) of human bone marrow-derived MSCs (Sittichokechaiwut et al. 2010), the resulting WSS would be between 4.12 and 7.18 mPa and thus well within the range to stimulate an osteogenic response. In addition, from an in vivo study by Duty et al. (2007), it was found that bone tissue formation and mineralisation were enhanced within a porous PLA scaffold ($p = 71\,\%$, $d = 397\,\mu$m) under dynamic compression with a compressive strain of 1.8 % and frequency of 1 Hz. According to our prediction, an average WSS around 2.0 mPa would result within the scaffold, which was within the range for stimulating the osteogenic response. These results suggest an important contribution of load-induced fluid shear stress within tissue engineering scaffolds under mechanical compression regimes.

Large pore sizes and scaffold porosities have been found to significantly enhance cell attachment, differentiation, proliferation and migration (Haugh et al. 2009; Kim et al. 2010; Murphy et al. 2010, 2013). According to our study, a larger pore size (i.e. $d \geq 300\,\mu m$) would result in a lower WSS, in particular for the highly porous scaffold (i.e. $p = 90\%$). For example, a dynamic cell culture study, in which bone cells seeded in a collagen–GAG scaffold were exposed to fluid perfusion (1 mL/min), suggested that larger pore sizes ($d = 325\,\mu m$) were preferable for mechanical stimulation for a better cell attachment, and an average WSS of 17.6 mPa resulted in the scaffold (McCoy et al. 2012). If the scaffolds were fabricated by rapid prototyping with spherical or cubical pores of $325\,\mu m$, an average WSS of 12.7 and 8.2 mPa would result for spherical and cubical architectures ($p = 90\%$) under a similar flow rate (1 mL/min). So, the WSS of the spherical scaffold ($p = 90\%$, $d = 325\,\mu m$) was within 28% of the WSS of the irregular-pore scaffold, which was preferable for cell attachment under mechanical stimulation (McCoy et al. 2012) and might be used under similar conditions to achieve a similar cell attachment with the irregular collagen–GAG scaffold. However, some other studies found that cells also could be stimulated to an osteogenic response in scaffolds with a smaller pore size. For instance, Gomes et al. used a scaffold with a small pore size ($d = 181\,\mu m$, $p = 75\%$) to stimulate bone marrow cells to an osteogenic response and observed increased ALP activity and calcium deposition under a flow rate of 0.3 mL/min (Gomes et al. 2003). According to the predictions of our models, the resulting average WSS would be 8.5 mPa (spherical architecture) and 6.0 mPa (cubical architecture), which are within the WSS range (0.1–10 mPa) for promoting osteogenesis. However, the findings in this study indicated that a larger pore size would result in more equally distributed WSS, especially in the spherical architecture. Therefore, considering all the factors mentioned above, a spherical-architecture scaffold with a large pore size (i.e. $d \geq 300\,\mu m$) is suggested to be more preferable for bone tissue engineering experiments.

Finally, the parametric variation study in this paper showed that under the compressive strain of 5% (1 Hz), the resulting WSS was comparable to that in the fluid perfusion system (inlet fluid velocity = 0.1 mm/s) (see Figs. 4 vs. 8, Figs. 5 vs. 9). However, from the perspective of cellular strain caused by mechanical compression of scaffold, a recent computational study discussed the limitation of mechanical compression that the bridged cells within scaffolds were less stimulated than the attached cells (Zhao et al. 2015). But under fluid perfusion, the bridged cells received higher stimulation than attached cells (Zhao et al. 2015). Our predictions for the combined loading condition revealed that the WSS varied from that in either fluid perfusion or mechanical compression system; moreover, it was amplified. Thus, combined loading could enhance stimulation on both bridged

and attached cells. To some extent, this was supported by tissue engineering experimental phenomena. For example, an experimental study showed that a combination of fluid perfusion (inlet flow rate: 10 mL/min) and mechanical compression (compressive strain: 10%) could stimulate the bone cells resulting in larger amount of osteocalcin and higher Runx2 expression than those under fluid perfusion after 2- to 3-week culture (Jagodzinski et al. 2008).

5 Conclusion

In this study, we investigated the influence of scaffold geometry (i.e. architecture, pore size and porosity) and external loading on the mechanical stimulation within scaffolds using a computational approach. The study of geometric variation was conducted for both fluid perfusion and mechanical compression loading, which were modelled by CFD and FSI methods, respectively. It was found that the pore size had a greater influence on mechanical stimulation within the scaffold than the architecture and porosity. A combination of fluid perfusion and mechanical compression with different profiles was also investigated using an FSI approach. Interestingly, the mechanical stimulation was amplified within the scaffold under combined loading, which indicated a better suitability for cell stimulation within a bone TE scaffold. Importantly, the results of this parametric study not only shed light on the mechanism of mechanical stimulation (in terms of WSS) within tissue-engineered (TE) scaffolds, but also derived an expression that can be applied by researchers in the design and optimisation of 3D TE scaffolds and experimental loading regimes so that a desired level of mechanical stimulation (WSS) is generated within the scaffold.

References

Altman GH et al (2002) Cell differentiation by mechanical stress. FASEB J 16:270–272. doi:10.1096/fj.01-0656fje

Angele P et al (2004) Cyclic, mechanical compression enhances chondrogenesis of mesenchymal progenitor cells in tissue engineering scaffolds. Biorheology 41:335–346

Bancroft GN, Sikavitsas VI, van den Dolder J, Sheffield TL, Ambrose CG, Jansen JA, Mikos AG (2002) Fluid flow increases mineralized matrix deposition in 3D perfusion culture of marrow stromal osteoblasts in a dose-dependent manner. Proc Natl Acad Sci USA 99:12600–12605. doi:10.1073/pnas.202296599

Blecha LD, Rakotomanana L, Razafimahery F, Terrier A, Pioletti DP (2010) Mechanical interaction between cells and fluid for bone tissue engineering scaffold: modulation of the interfacial shear

stress. J Biomech 43:933–937. doi:10.1016/j.jbiomech.2009.11.004

Bliss CL, Szivek JA, Tellis BC, Margolis DS, Schnepp AB, Ruth JT (2007) Sensate scaffolds can reliably detect joint loading. J Biomed Mater Res B 81B:30–39. doi:10.1002/Jbm.B.30632

Bose S, Vahabzadeh S, Bandyopadhyay A (2013) Bone tissue engineering using 3D printing. Mater Today 16:496–504. doi:10.1016/j.mattod.2013.11.017

Chowdhury TT, Schulz RM, Rai SS, Thuemmler CB, Wuestneck N, Bader A, Homandberg GA (2010) Biomechanical modulation of collagen fragment-induced anabolic and catabolic activities in chondrocyte/agarose constructs. Arthr Res Ther 12:R82. doi:10.1186/ar3009

Delaine-Smith RM, Reilly GC (2012) Mesenchymal stem cell responses to mechanical stimuli. Muscles Ligaments Tendons J 2:169–180

Dowling EP, McGarry JP (2014) Influence of spreading and contractility on cell detachment. Ann Biomed Eng 42:1037–1048. doi:10.1007/s10439-013-0965-5

Duty AO, Oest ME, Guldberg RE (2007) Cyclic mechanical compression increases mineralization of cell-seeded polymer scaffolds in vivo. J Biomech Eng 129:531–539. doi:10.1115/1.2746375

Georgiou G, Mathieu L, Pioletti DP, Bourban PE, Manson JA, Knowles JC, Nazhat SN (2007) Polylactic acid-phosphate glass composite foams as scaffolds for bone tissue engineering. J Biomed Mater Res Part B Appl Biomater 80:322–331. doi:10.1002/jbm.b.30600

Goldstein AS, Juarez TM, Helmke CD, Gustin MC, Mikos AG (2001) Effect of convection on osteoblastic cell growth and function in biodegradable polymer foam scaffolds. Biomaterials 22:1279–1288

Gomes ME, Sikavitsas VI, Behravesh E, Reis RL, Mikos AG (2003) Effect of flow perfusion on the osteogenic differentiation of bone marrow stromal cells cultured on starch-based three-dimensional scaffolds. J Biomed Mater Res Part A 67:87–95. doi:10.1002/jbm.a.10075

Grayson WL, Bhumiratana S, Cannizzaro C, Chao PH, Lennon DP, Caplan AI, Vunjak-Novakovic G (2008) Effects of initial seeding density and fluid perfusion rate on formation of tissue-engineered bone. Tissue Eng Part A 14:1809–1820. doi:10.1089/ten.tea.2007.0255

Gross KA, Rodriguez-Lorenzo LM (2004) Biodegradable composite scaffolds with an interconnected spherical network for bone tissue engineering. Biomaterials 25:4955–4962. doi:10.1016/j.biomaterials.2004.01.046

Harley BA, Leung JH, Silva ECCM, Gibson LJ (2007) Mechanical characterization of collagen-glycosaminoglycan scaffolds. Acta Biomater 3:463–474. doi:10.1016/j.aetbio.2006.12.009

Harley BAC, Kim HD, Zaman MH, Yannas IV, Lauffenburger DA, Gibson LJ (2008) Microarchitecture of three-dimensional scaffolds influences cell migration behavior via junction interactions. Biophys J 95:4013–4024. doi:10.1529/biophysj.107.122598

Haugh MG, Jaasma MJ, O'Brien FJ (2009) The effect of dehydrothermal treatment on the mechanical and structural properties of collagen-GAG scaffolds. J Biomed Mater Res Part A 89:363–369. doi:10.1002/jbm.a.31955

Hendrikson WJ, van Blitterswijk CA, Verdonschot N, Moroni L, Rouwkema J (2014) Modeling mechanical signals on the surface of microCT and CAD based rapid prototype scaffold models to predict (early stage) tissue development. Biotechnol Bioeng 111:1864–1875. doi:10.1002/bit.25231

Hollister SJ (2005) Porous scaffold design for tissue engineering. Nat Mater 4:518–524. doi:10.1038/Nmat1421

Hou GN, Wang J, Layton A (2012) Numerical methods for fluid-structure interaction: a review. Commun Comput Phys 12:337–377. doi:10.4208/cicp.291210.290411s

Hutmacher DW (2000) Scaffolds in tissue engineering bone and cartilage. Biomaterials 21:2529–2543

Jaasma MJ, O'Brien FJ (2008) Mechanical stimulation of osteoblasts using steady and dynamic fluid flow. Tissue Eng Part A 14:1213–1223

Jagodzinski M et al (2008) Influence of perfusion and cyclic compression on proliferation and differentiation of bone marrow stromal cells in 3-dimensional culture. J Biomech 41:1885–1891. doi:10.1016/j.jbiomech.2008.04.001

Jungreuthmayer C, Donahue SW, Jaasma MJ, Al-Munajjed AA, Zanghellini J, Kelly DJ, O'Brien FJ (2009a) A comparative study of shear stresses in collagen-glycosaminoglycan and calcium phosphate scaffolds in bone tissue-engineering bioreactors. Tissue Eng Part A 15:1141–1149. doi:10.1089/ten.tea.2008.0204

Jungreuthmayer C, Jaasma MJ, Al-Munajjed AA, Zanghellini J, Kelly DJ, O'Brien FJ (2009b) Deformation simulation of cells seeded on a collagen-GAG scaffold in a flow perfusion bioreactor using a sequential 3D CFD-elastostatics model. Med Eng Phys 31:420–427. doi:10.1016/j.medengphy.2008.11.003

Karamichos D, Skinner J, Brown R, Mudera V (2008) Matrix stiffness and serum concentration effects matrix remodelling and ECM regulatory genes of human bone marrow stem cells. J Tissue Eng Regen Med 2:97–105. doi:10.1002/term.69

Karande TS, Ong JL, Agrawal CM (2004) Diffusion in musculoskeletal tissue engineering scaffolds: design issues related to porosity, permeability, architecture, and nutrient mixing. Ann Biomed Eng 32:1728–1743

Keogh MB, O'Brien FJ, Daly JS (2010) Substrate stiffness and contractile behaviour modulate the functional maturation of osteoblasts on a collagen-GAG scaffold. Acta Biomater 6:4305–4313. doi:10.1016/j.actbio.2010.06.001

Keogh MB, Partap S, Daly JS, O'Brien FJ (2011) Three hours of perfusion culture prior to 28 days of static culture, enhances osteogenesis by human cells in a collagen GAG scaffold. Biotechnol Bioeng 108:1203–1210

Kerckhofs G, Pyka G, Loeckx D, Van Bael S, Schrooten J, Wevers M (2010) The combined use of micro-CT imaging, in-situ loading and non-rigid image registration for 3D experimental local strain mapping on porous bone tissue engineering scaffolds under compressive loading. In: European conference for non-destructive testing (ECNDT) 2010, Moscow, Russia, 7–11 June 2010

Kim K, Yeatts A, Dean D, Fisher JP (2010) Stereolithographic bone scaffold design parameters: osteogenic differentiation and signal expression. Tissue Eng Part B Rev 16:523–539. doi:10.1089/ten.TEB.2010.0171

Liu C et al (2012a) Influence of perfusion and compression on the proliferation and differentiation of bone mesenchymal stromal cells seeded on polyurethane scaffolds. Biomaterials 33:1052–1064. doi:10.1016/j.biomaterials.2011.10.041

Liu LY et al (2012b) Different effects of intermittent and continuous fluid shear stresses on osteogenic differentiation of human mesenchymal stem cells. Biomech Model Mechan 11:391–401

Marin AC, Lacroix D (2015) The inter-sample structural variability of regular tissue-engineered scaffolds significantly affects the micromechanical local cell environment. Interface Focus 5

McCoy RJ, Jungreuthmayer C, O'Brien FJ (2012) Influence of flow rate and scaffold pore size on cell behavior during mechanical stimulation in a flow perfusion bioreactor. Biotechnol Bioeng 109:1583–1594. doi:10.1002/Bit.24424

Melchels FPW et al (2011) The influence of the scaffold design on the distribution of adhering cells after perfusion cell seeding. Biomaterials 32:2878–2884. doi:10.1016/j.biomaterials.2011.01.023

Milan JL, Planell JA, Lacroix D (2010) Simulation of bone tissue formation within a porous scaffold under dynamic compression. Biomech Model Mechanobiol 9:583–596. doi:10.1007/s10237-010-0199-5

Miyashita S et al (2014) Mechanical forces induce odontoblastic differentiation of mesenchymal stem cells on three-dimensional

biomimetic scaffolds. J Tissue Eng Regen Med. doi:10.1002/term.1928

Mullen CA, Vaughan TJ, Billiar KL, McNamara LM (2015) The effect of substrate stiffness, thickness, and cross-linking density on osteogenic cell behavior. Biophys J 108:1604–1612. doi:10.1016/j.bpj.2015.02.022

Mullen CA, Vaughan TJ, Voisin MC, Brennan MA, Layrolle P, McNamara LM (2014) Cell morphology and focal adhesion location alters internal cell stress. J R Soc Interface 11:20140885. doi:10.1098/rsif.2014.0885

Murphy CM, Haugh MG, O'Brien FJ (2010) The effect of mean pore size on cell attachment, proliferation and migration in collagen-glycosaminoglycan scaffolds for bone tissue engineering. Biomaterials 31:461–466. doi:10.1016/j.biomaterials.2009.09.063

Murphy CM, Matsiko A, Haugh MG, Gleeson JP, O'Brien FJ (2012) Mesenchymal stem cell fate is regulated by the composition and mechanical properties of collagen-glycosaminoglycan scaffolds. J Mech Behav Biomed 11:53–62. doi:10.1016/j.jmbbm.2011.11.009

Murphy CM, O'Brien FJ, Little DG, Schindeler A (2013) Cell-scaffold interactions in the bone tissue engineering triad. Eur Cells Mater 26:120–132

Olivares AL, Marsal E, Planell JA, Lacroix D (2009) Finite element study of scaffold architecture design and culture conditions for tissue engineering. Biomaterials 30:6142–6149. doi:10.1016/j.biomaterials.2009.07.041

Porter B, Zauel R, Stockman H, Guldberg R, Fyhrie D (2005) 3-D computational modeling of media flow through scaffolds in a perfusion bioreactor. J Biomech 38:543–549. doi:10.1016/j.jbiomech.2004.04.011

Sandino C, Planell JA, Lacroix D (2008) A finite element study of mechanical stimuli in scaffolds for bone tissue engineering. J Biomech 41:1005–1014. doi:10.1016/j.jbiomech.2007.12.011

Schulz RM, Wustneck N, van Donkelaar CC, Shelton JC, Bader A (2008) Development and validation of a novel bioreactor system for load- and perfusion-controlled tissue engineering of chondrocyte-constructs. Biotechnol Bioeng 101:714–728. doi:10.1002/bit.21955

Shin J, Kim S, Jeong D, Lee HG, Lee D, Lim JY, Kim J (2012) Finite element analysis of Schwarz P surface pore geometries for tissue-engineered scaffolds. Math Probl Eng 13. doi:10.1155/2012/694194

Silva MM et al (2006) The effect of anisotropic architecture on cell and tissue infiltration into tissue engineering scaffolds. Biomaterials 27:5909–5917. doi:10.1016/j.biomaterials.2006.08.010

Sittichokechaiwut A, Edwards JH, Scutt AM, Reilly GC (2010) Short bouts of mechanical loading are as effective as dexamethasone at inducing matrix production by human bone marrow mesenchymal stem cell. Eur Cells Mater 20:45–57

Smith IO, Ma PX (2010) Cell and biomolecule delivery for regenerative medicine. Sci Technol Adv Mat 11: doi:10.1088/1468-6996/11/1/014102

Stops AJ, Heraty KB, Browne M, O'Brien FJ, McHugh PE (2010) A prediction of cell differentiation and proliferation within a collagen-glycosaminoglycan scaffold subjected to mechanical strain and perfusive fluid flow. J Biomech 43:618–626. doi:10.1016/j.jbiomech.2009.10.037

Subramony SD, Dargis BR, Castillo M, Azeloglu EU, Tracey MS, Su A, Lu HH (2013) The guidance of stem cell differentiation by substrate alignment and mechanical stimulation. Biomaterials 34:1942–1953. doi:10.1016/j.biomaterials.2012.11.012

Tai H et al (2007) Control of pore size and structure of tissue engineering scaffolds produced by supercritical fluid processing: discussion with reviewers. Eur Cells Mater 14:76–77

Tan Q, Li S, Ren J, Chen C (2011) Fabrication of porous scaffolds with a controllable microstructure and mechanical properties by porogen fusion technique. Int J Mol Sci 12:890–904. doi:10.3390/ijms12020890

Tang Y, Wong C, Wang H, Sutti A, Kirkland M, Wang X, Lin T (2011) Three-dimensional tissue scaffolds from interbonded poly(epsilon-caprolactone) fibrous matrices with controlled porosity. Tissue Eng Part C Methods 17:209–218. doi:10.1089/ten.TEC.2010.0223

Thompson MS, Epari DR, Bieler F, Duda GN (2010) In vitro models for bone mechanobiology: applications in bone regeneration and tissue engineering. Proc Inst Mech Eng Part H J Eng Med 224:1533–1541

Tuan HS, Hutmacher DW (2005) Application of micro CT and computation modeling in bone tissue engineering. Comput Aided Des 37:1151–1161. doi:10.1016/j.cad.2005.02.006

Vance J, Galley S, Liu DF, Donahue SW (2005) Mechanical stimulation of MC3T3 osteoblastic cells in a bone tissue-engineering bioreactor enhances prostaglandin E2 release. Tissue Eng 11:1832–1839. doi:10.1089/ten.2005.11.1832

Wang YK, Chen CS (2013) Cell adhesion and mechanical stimulation in the regulation of mesenchymal stem cell differentiation. J Cell Mol Med 17:823–832. doi:10.1111/jcmm.12061

Widmer MS et al (1998) Manufacture of porous biodegradable polymer conduits by an extrusion process for guided tissue regeneration. Biomaterials 19:1945–1955. doi:10.1016/S0142-9612(98)00099-4

Yu X, Botchwey EA, Levine EM, Pollack SR, Laurencin CT (2004) Bioreactor-based bone tissue engineering: the influence of dynamic flow on osteoblast phenotypic expression and matrix mineralization. Proc Natl Acad Sci USA 101:11203–11208. doi:10.1073/pnas.0402532101

Zhao F, Vaughan TJ, McNamara LM (2015) Multiscale fluid-structure interaction modelling to determine the mechanical stimulation of bone cells in a tissue engineered scaffold. Biomech Model Mechanobiol 14:231–243. doi:10.1007/s10237-014-0599-z